

# High-OAM Deep Ultraviolet Twisted Light Generation for RF-Photoinjector Applications\*

A.S. Dyatlov<sup>1,2,†</sup>, D.M. Dolgintsev<sup>1</sup>, V.V. Gerasimov<sup>3,4</sup>, V.V. Kobets<sup>2</sup>, V.P. Nazmov<sup>3,5</sup>, M.A. Nozdrin<sup>2</sup>, A.N. Sergeev<sup>1</sup>, D.S. Shokin<sup>2</sup>, K.E. Yunenko<sup>2</sup>, and D.V. Karlovets<sup>1,6</sup>

<sup>1</sup> *School of Physics and Engineering, ITMO University, 9 Lomonosova St., Saint-Petersburg, 191002, Russia*

<sup>2</sup> *Joint Institute for Nuclear Research, 6 Joliot-Curie St., Dubna, 141980, Moscow Region, Russia*

<sup>3</sup> *Budker Institute of Nuclear Physics, Siberian Branch of RAS, 11, Acad. Lavrentieva Pr., Novosibirsk, 630090, Russia*

<sup>4</sup> *Department of Physics, Novosibirsk State University, 1, Pirogova St., Novosibirsk, 630090, Russia*

<sup>5</sup> *Institute of Solid State Chemistry and Mechanochemistry, Siberian Branch of RAS, 18, Kutateladze St., Novosibirsk, 630090, Russia*

<sup>6</sup> *Petersburg Nuclear Physics Institute of NRC "Kurchatov Institute", 1, mkr. Orlova roshcha, Gatchina, Leningradskaya Oblast, 188300, Russia*

## Abstract

The generation of relativistic vortex electron beams via photoemission requires ultraviolet laser beams with well-controlled orbital angular momentum (OAM) and compatibility with radio-frequency (RF) photoinjector drive-laser systems. High-OAM vortex beams at a wavelength of 266 nm are generated using three fabricated diffractive optical elements integrated into an operational photoinjector beamline: a reflective fork grating, a high-topological-charge spiral phase plate, and binary axicons. The spiral phase plate produces a high-purity Laguerre–Gaussian mode with an OAM of  $\ell = 64\hbar$  and a conversion efficiency of 80%, whereas binary axicons generate low-divergence quasi-Bessel beams forming a superposition of multiple OAM states with a finite OAM bandwidth imposed by their binary phase structure. Fork gratings provide flexible access to lower OAM values and enable robust modal diagnostics. The generated beams are characterized using cylindrical-lens mode conversion and radial intensity analysis, demonstrating practical control of both the OAM content and spectral bandwidth of ultraviolet structured light for accelerator-based applications.

## 1 Introduction

Optical beams of the so-called twisted light [2, 3, 4, 5, 6, 7, 8, 9, 10], carrying orbital angular momentum (OAM) play an increasingly important role in modern photonics, enabling advanced control of light–matter interactions [11], high-dimensional quantum communication protocols [12, 13, 14], and structured-beam excitation in electron and plasma systems [15]. Generating well-defined OAM modes in the deep ultraviolet (UV) range is particularly relevant for photocathode-based electron sources [5, 7, 8, 9, 16] and nonlinear UV photonics, where high spatial coherence, low divergence, and precise transverse-mode control are required.

\*This document is the results of the research project funded by the Russian Science Foundation (Project No. 23-62-10026) [1]

†Email: [aleksandr.dyatlov@metalab.ifmo.ru](mailto:aleksandr.dyatlov@metalab.ifmo.ru)

However, producing stable high-charge OAM beams in the deep UV remains technically challenging. Spatial light modulators and digital micromirror devices, widely used at visible wavelengths, suffer from strong absorption, laser-induced damage, and low diffraction efficiency in the UV range. Binary spiral zone plates (SZPs) operate in this spectral range but are intrinsically limited to about 40% conversion efficiency [17]. Classical fork gratings [18] can offer higher efficiency, yet they restrict the accessible OAM values to integer multiples of the diffraction order and often require tight focusing. Spiral phase plates (SPPs), while conceptually ideal for generating arbitrary OAM values [19], demand nanometer-scale surface accuracy over millimeter-sized apertures [20] and must withstand significant UV fluence. Binary axicons, widely used to generate Bessel-like twisted light (vortex) [21, 22, 23], provide robustness and tunability but introduce characteristic ring fragmentation due to their discretized phase profiles. As a consequence, none of these approaches alone provides a universal, high-fidelity, UV-compatible solution for high-order OAM generation.

In this work, we demonstrate the generation of deep-ultraviolet twisted light using three fabricated diffractive optical elements (DOEs): reflective fork gratings, high topological charge spiral phase plate, and binary axicons, all integrated into a drive-laser system of an RF-photoinjector [24]. We generate Laguerre–Gaussian (LG) modes with the OAM values up to  $\ell = 64\hbar$ , verify their modal structure using cylindrical-lens mode conversion, and compare the measured intensity distributions with numerical simulations. In contrast, binary axicons produce low-divergence quasi-Bessel beams whose OAM content forms a superposition of multiple topological charges, reflecting the binary radial phase modulation. The generated beams exhibit high spatial fidelity, stable operation under UV irradiation, and low divergence suitable for photocathode illumination. The fabrication techniques used here rely on robust, scalable processes compatible with fused silica, SU-8 resists, and metal-coated substrates, enabling durable large-aperture UV optics.

To the best of our knowledge, this is the first comprehensive experimental demonstration of the deep-UV high-OAM beams produced using several types of fabricated DOEs and validated through the mode-conversion diagnostics. These results are directly relevant for the next-generation accelerator facilities with the so-called vortex electrons - massive counterparts of twisted photons. Relativistic vortex electrons are attracting increasing interest in nuclear and hadronic physics, where OAM offers a new degree of freedom for probing spin-structure phenomena and may complement the conventional spin-polarized beams [7, 9, 25, 26, 27]. Structured photocathode illumination is likewise becoming important for accelerator-based light sources, including polarized synchrotron-radiation facilities, free-electron lasers, and Compton  $\gamma$ -ray sources, all of which benefit from precise control of the transverse phase space of the injected electrons. The demonstrated deep-UV high-OAM beam generation thus can provide [1] a practical route toward the realization of MeV-scale vortex electrons in modern high-brightness photoinjectors.

## 2 Design and fabrication of high-OAM diffractive optical elements

### 2.1 A reflective diffraction fork grating with a topological charge $m = 2$

A fork grating introduces a phase dislocation of topological charge  $m$ , generating optical vortices in the diffracted orders. The phase profile employed in this work follows Ref. [2]:

$$\Phi(x, y) = 2\pi \frac{x}{x_0} + m \arctan \frac{y}{x}, \quad (1)$$

where  $x_0$  denotes the grating period. The continuous phase distribution is converted into a binary mask by applying a cosine-based threshold function,

$$B(x, y) = \begin{cases} 1, & M(x, y) > T, \\ 0, & M(x, y) \leq T. \end{cases} \quad (2)$$

with the modulation function defined as

$$M(x, y) = \frac{1}{2} \alpha [1 + \cos \Phi(x, y)]. \quad (3)$$

In this context, the topological charge of the grating  $m$  is the number of  $2\pi$  phase windings embedded into the grating period. When a Gaussian beam is diffracted, each diffraction order acquires an optical vortex with topological charge of the beam [28]

$$\ell = n \cdot m. \quad (4)$$

where  $n$  is the diffraction order. The vortex charge  $\ell$  defines the OAM carried by the beam, with each photon transferring  $\ell\hbar$  of the OAM.

The resulting binary mask is shown in Figure 1. The pattern was transferred onto an aluminum mirror via laser engraving, yielding a reflective grating with a  $1 \times 1$  mm active area and a spatial resolution of approximately  $30 \mu\text{m}$ . A microscope image of the fabricated device is presented in Figure 2.

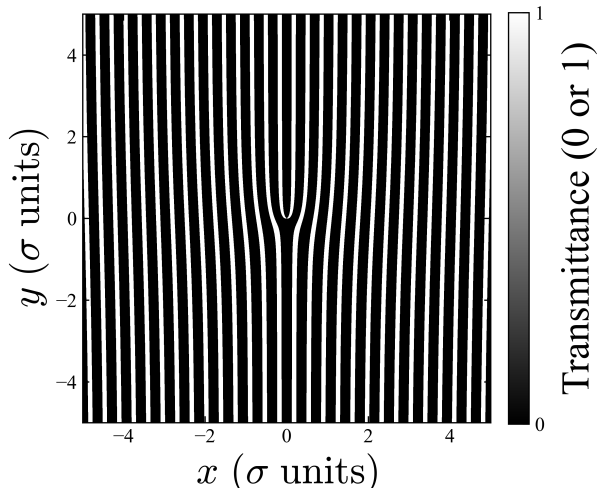


**Figure 1:** A Binarized fork-grating mask generated according to Eq. 1. The grayscale corresponds to binary transmittance values (0 or 1). Coordinates are shown in normalized units.

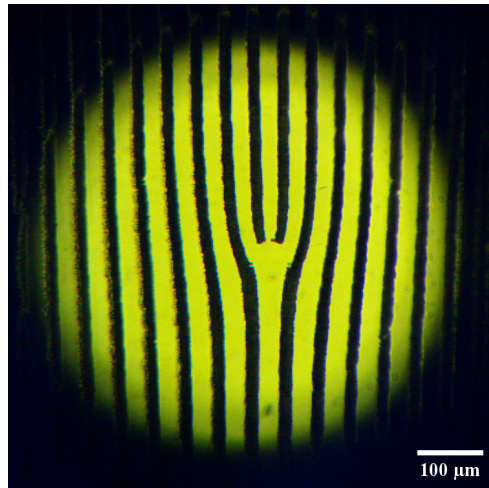


**Figure 2:** A microscope image of the reflective fork-grating laser-engraved on an aluminum-mirror substrate. The fabricated structure reproduces the binary mask of Figure 1. The active area is  $1 \times 1$  mm with a spatial resolution of  $30 \mu\text{m}$ .

## 2.2 A spiral phase plate with a topological charge $m = 64$

A spiral phase plate (SPP) generates an azimuthally varying phase through a helical surface relief. The phase shift introduced by the plate is given by [20]

$$\varphi_0(\theta) = \frac{2\pi}{\lambda} \left[ (n - n_0) \frac{h_s \theta}{2\pi} + n h_0 \right], \quad (5)$$

where  $n$  and  $n_0$  are the refractive indices of the plate material and the surrounding medium, respectively;  $h_0$  is the base thickness;  $h_s$  is the total height variation over a full  $2\pi$  rotation; and  $\theta$  is the azimuthal angle. The corresponding surface profile is

$$h(\theta) = h_s \frac{\theta}{2\pi} + h_0. \quad (6)$$

To generate a twisted light with an OAM  $\ell$ , the phase must increase by  $2\pi m$  over one full revolution:

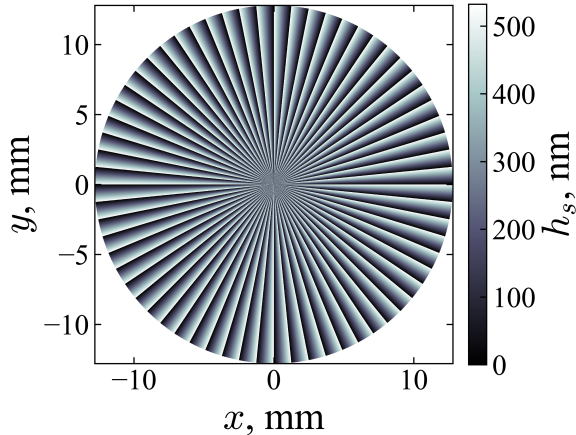
$$\varphi_0(\theta) = \ell\theta + \frac{2\pi n h_0}{\lambda}. \quad (7)$$

For UV operation at  $\lambda = 266$  nm using fused silica ( $n = 1.49$ ), the required total height variation is approximately  $h_s \approx 34 \mu\text{m}$ . Implementing a topological charge of  $m = 64$  is achieved by dividing the spiral into 64 discrete azimuthal sectors, each introducing a  $2\pi$  phase step. This corresponds to a height increment of about 532 nm per sector. The resulting two-dimensional phase topology is shown in Figure 3.

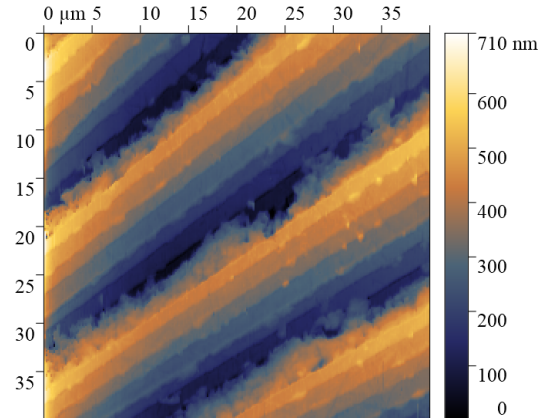
The SPP was fabricated in fused silica using multi-level photolithography followed by high-precision plasma etching (Holo/Or, Israel). This manufacturing process is commonly employed for diffractive optical elements and provides the required micron-scale surface relief and sub-micron accuracy of the phase profile, ensuring stable performance under high-intensity UV illumination [29, 30, 31, 32].

Figure 4 shows the measured surface profile of the fabricated SPP obtained using an AIST-NT SmartSPM 1000 atomic force microscope (AFM). The AFM image reveals that small dust particles

accumulated inside the narrow gaps between adjacent sectors during handling, although this contamination did not affect the quality of the generated twisted light. A weak striped pattern is also visible across the sectors, originating from layer-by-layer etching into the fused-silica substrate. Despite this fine structuring, the average step height remains close to 500 nm, which is in good agreement with the designed two-dimensional topological phase map.



**Figure 3:** Two-dimensional phase topology of the spiral phase plate (SPP) featuring 64 azimuthal steps within an aperture of  $D = 25.6$  mm. The topological charge is  $m = 64$ . The step height is  $h_s \approx 532$  nm, calculated for  $\lambda = 266$  nm and  $n = 1.49$ .



**Figure 4:** The atomic force microscope image of the fabricated SPP. Dust particles trapped between the etched sectors and the striped etching pattern do not degrade the beam quality. The measured step height is  $\sim 500$  nm, consistent with the design.

### 2.3 Binary axicons with the topological charge $m = 3$ and 10

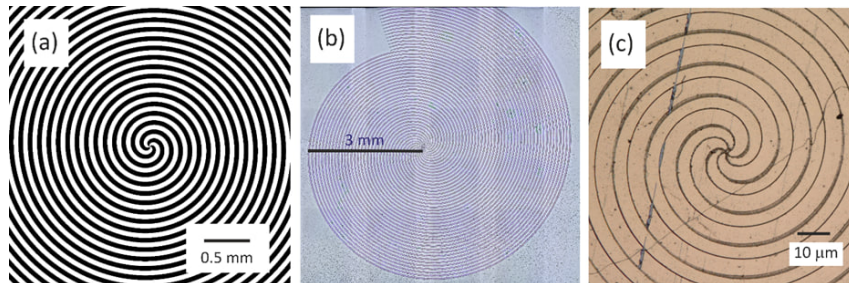


**Figure 5:** (a) Phase mask of an axicon with topological charge  $m = 3$ . The micrograph of a binary planar axicon with an aperture diameter of 6 mm and  $m = 3$  in a SU-8 photoresist layer; (b) full view; (c) enlarged view obtained in refractive mode, covered with a gold layer

Bessel beams were modeled using the Wave-ThruMasks MATLAB package [33], which computes field propagation through transparent phase elements within the scalar diffraction theory using the Rayleigh-Sommerfeld integral [34]. The binary phase distribution used to generate twisted light Bessel beams is

$$H(r, \varphi) = F(\ell\varphi - kr) = \frac{\pi}{2} \times \text{sign}[\sin(m\varphi - kr)], \quad (8)$$

where  $m$  is the topological charge,  $\varphi$  the azimuthal angle,  $k$  the radial wave number, and  $r = \sqrt{x^2 + y^2}$ . An example mask for  $m = 3$  is shown in Figure 5(a).

Binary axicon topologies in the form of Archimedean spirals with  $m = 3$  and  $m = 10$  and a period of  $p = 100 \mu\text{m}$  were generated in MathCad. The rendering process was terminated once the spirals reached the working aperture of 6 mm.

The encoded topology was first transferred onto a glass photomask in an iron-oxide layer. The axicons were then fabricated via photolithography in SU-8 photoresist deposited on leucosapphire substrates, which provide high ultraviolet transmittance. The polymer crosslinked network of SU-8 also offers high

resistance to ionizing radiation [35]. Prior to resist deposition, the substrates were cleaned sequentially in acetone and in a 5% aqueous sulfuric-acid solution. To achieve the required film thickness, SU-8 2002 resist was diluted with an SU-8 2000 thinner.

The required binary layer thickness is

$$h = \frac{\lambda}{2(n-1)}, \quad (9)$$

where  $n \approx 1.66$  is the refractive index of SU-8. For  $\lambda = 266$  nm, this yields  $h \approx 200$  nm, providing the necessary  $\pi$  phase shift.

The photoresist was applied using a spin coater operated at 3000 rpm. The resulting film was soft-baked on a hotplate at  $95^\circ\text{C}$  for 5 minutes. The axicon pattern was transferred using a custom UV exposure system based on an H44TV1C0-LFVY LED lamp operating at a wavelength of 365 nm, with an exposure time of 23 minutes. After a post-exposure bake at  $95^\circ\text{C}$  for 5 minutes and development for 1.5 minutes in PGMEA, the resist thickness was measured with a Linnik MII-4 interference microscope with an accuracy of  $\pm 15$  nm. Figures 5(b-c) show the resulting axicon relief.

### 3 Numerical simulation of the generated beams

Numerical simulation of the fork grating and the SPP was performed using a standard angular-spectrum propagation framework [34]. A Gaussian input beam was assumed and multiplied by the corresponding phase profile of the diffractive optical element:  $\Phi(x, y)$  for the fork grating (Eq. 1) and  $\varphi_0(\theta)$  for the SPP (Eq. 5). Free-space propagation and lens transformations were implemented using Fourier-domain transfer operators.

To suppress boundary effects and residual on-axis intensity that become pronounced for high-OAM modes, a radial apodization was applied, introducing an outer truncation and a central suppression region. The specific functional form was chosen to minimize numerical artifacts without affecting the intrinsic transverse mode structure.

This modeling procedure enables direct comparison between the fork-grating-generated and SPP-generated beams, including verification of the expected OAM values. The simulated output patterns are shown in Figs. 6 and 7.

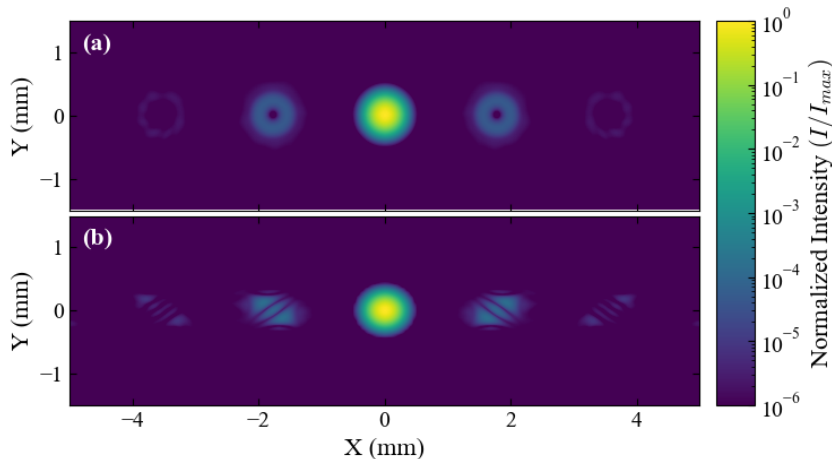


**Figure 6:** Simulation of the twisted light generation using the fork grating. (a) Transformation of the Gaussian input into the Laguerre–Gaussian modes carrying the OAM  $\ell = 0, \pm 2, \pm 4$ . (b) Corresponding cylindrical-lens mode conversion into the Hermite–Gaussian modes of the orders  $N = 1, 3, 5$ .

Similarly to the Laguerre–Gaussian simulations, quasi–Bessel beams produced in the focal region of the fabricated axicons were numerically modeled following the methodology of Ref. [23]. The results are shown in Figure 8. For all topological charge values, the characteristic ring-shaped intensity distribution is reproduced, consisting of  $m$  localized bright lobes whose number corresponds to the topological charge of each axicon. Small parasitic background features appear as weak spiral-like artifacts.

We also note that the binary phase pattern can lead to an effective interference of several overlapping wave components carrying slightly different OAMs. In this interpretation, the quasi–Bessel field can be viewed not as a single-mode vortex, but as a superposition of nearby OAM states [36, 37, 38]. The

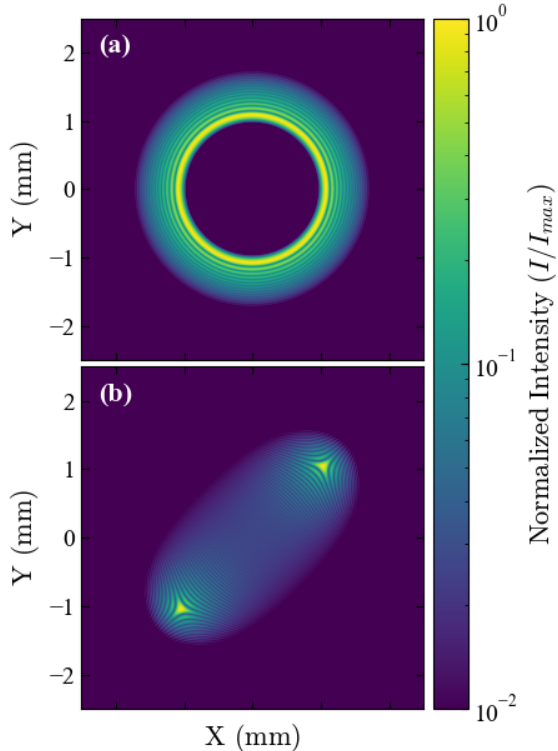


**Figure 7:** Simulation of twisted light generation using the designed SPP. (a) Transformation of a Gaussian input into the Laguerre–Gaussian mode carrying the OAM  $\ell = 64$ . (b) Cylindrical-lens conversion into the corresponding Hermite–Gaussian mode of the order  $N = 65$ .

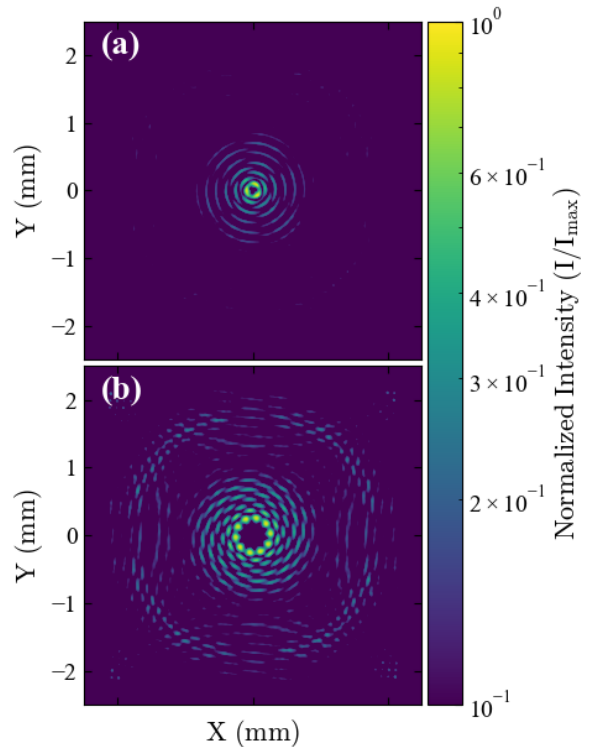


**Figure 8:** Simulated quasi-Bessel beams generated by binary axicons with topological charges  $m = 3$  and  $10$  (left to right). Each pattern exhibits an  $m$ -lobe intensity ring, while the binary phase structure leads to a segmented rather than continuous ring profile.

average topological charge would still correspond to the design value  $m$ , while the OAM can exhibit a finite dispersion [39], defining an effective OAM bandwidth. This qualitative picture is consistent with the observed fragmented ring structure and is commonly discussed for binary axicons.

In contrast, an ideal (non-binary) axicon produces a continuous, smooth ring [21]. In the present case, the discretization inherent to the binary phase patterns results in a fragmented ring composed of distinct intensity maxima, consistent with the expected behavior of binary axicons.

### 3.1 OAM spectrum decomposition

To quantify the OAM content of the generated fields, we project the numerically obtained complex transverse field onto azimuthal harmonics  $\exp(i\ell\varphi)$  [40, 41]. The projection coefficient is evaluated as

$$c_\ell \propto \int E(r, \varphi) \exp(-i\ell\varphi) W(r) r dr d\varphi, \quad (10)$$

where  $W(r)$  accounts for the finite aperture. The normalized spectrum is defined as

$$P_\ell = |c_\ell|^2 \quad \sum_\ell P_\ell = 1. \quad (11)$$

For Laguerre–Gaussian-like beams generated by fork gratings and spiral phase plates, the field contains a single azimuthal phase factor  $\exp(i\ell_0\varphi)$ . Owing to the orthogonality of azimuthal harmonics, only  $\ell = \ell_0$  survives upon integration, yielding a narrow single-peaked OAM spectrum (Figure 9(a–b)). In fork gratings, different diffraction orders carry distinct, well-defined topological charges, producing separated peaks at  $\ell = \pm 2, \pm 4, \text{ and } \pm 8$ .

In contrast, binary axicons generate quasi-Bessel beams with coupled radial and azimuthal structures. The field can be represented as a superposition of opposite OAM components  $\pm\ell$  whose weights vary with

radius [42, 43]. As a result, the azimuthal projection yields multiple non-vanishing components and a broadened OAM spectrum with a finite intrinsic bandwidth (Figure 9(c-d)).

To reduce numerical cancellation caused by rapid radial phase oscillations, the aperture is divided into  $N$  concentric annuli, within which local projections  $c_\ell^{(j)}$  are evaluated and summed as

$$P_\ell = \sum_j |c_\ell^{(j)}|^2. \quad (12)$$

This procedure preserves the physical OAM content while improving numerical stability.

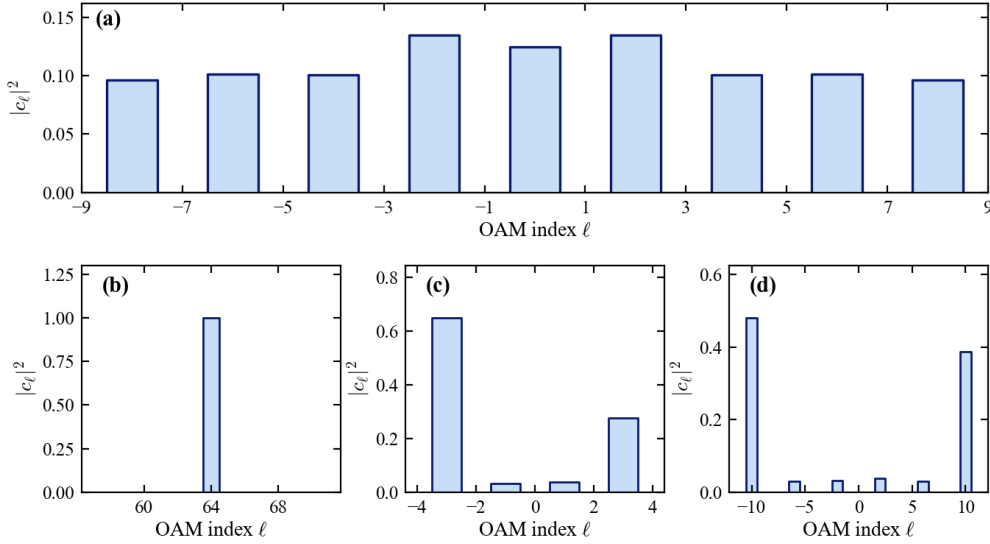


**Figure 9:** Orbital angular momentum (OAM) spectrum of the generated beams obtained by numerical projection onto azimuthal harmonics. (a) Fork grating: discrete, well-separated peaks at  $\ell = \pm 2, \pm 4$ , and  $\pm 8$ , corresponding to the individual diffraction orders of the grating and indicating high OAM spectral purity. (b) Spiral phase plate (SPP): a single narrow peak centered at the design topological charge, demonstrating the generation of a nearly pure OAM eigenstate. (c) Binary axicon with topological order  $m = 3$  and (d) binary axicon with  $m = 10$ : broadened and structured OAM spectra resulting from a superposition of multiple azimuthal harmonics with opposite topological charges, characteristic of quasi-Bessel beams.

### 3.2 Control of mode purity in beams generated by a binary axicons

As shown in Figure 9(a-b), fork gratings and spiral phase plates generate nearly pure OAM eigenstates. In contrast, binary spiral axicons produce coherent superpositions of azimuthal harmonics, leading to intrinsically mixed OAM spectrum.

The modal composition can be tuned by varying the transverse period  $p$  or SU-8 layer thickness  $h$  (Figures 10, 11). Decreasing  $p$  enhances the dominance of a single  $\ell$  component; however, the fabricated value  $p = 100 \mu\text{m}$  was chosen to obtain a focal spot of several hundred micrometers required for the photoemission experiment. A smaller period would increase the transverse spatial frequency and substantially enlarge the focal spot size in our geometry. Consequently, in the deep-ultraviolet diffraction regime considered here, the axicon mostly generates a superposition of pure OAM states with dominant  $\pm\ell$  components or their symmetric superposition.

Variation of the thickness  $h$  modifies the effective complex transmission function of the axicon and leads to the appearance of a non-negligible  $\ell = 0$  contribution in the OAM spectrum (Figure 11). Even changes of several tens of nanometers noticeably reduce the modal purity. This behavior originates from deviations of the phase modulation from its optimal value combined with amplitude modulation introduced by the finite conductivity of the metal. In the experiment, such a contribution would manifest itself as a Gaussian-like on-axis intensity core superimposed on the annular Bessel structure.

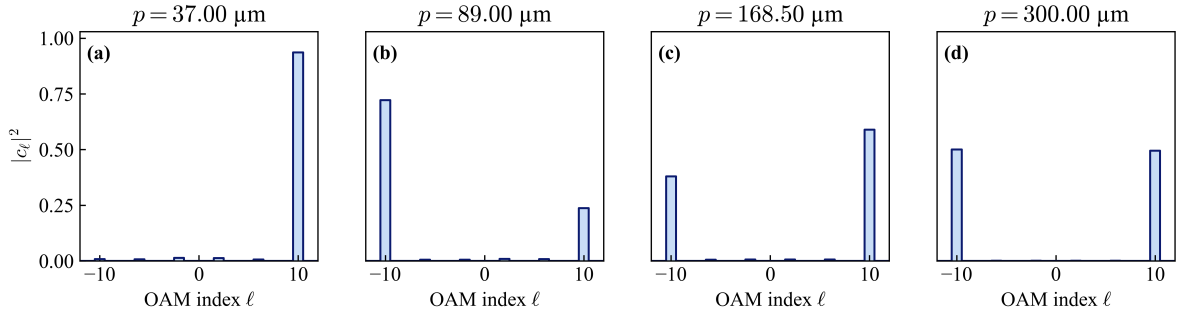


**Figure 10:** Projected OAM spectra  $|c_\ell|^2$  of the field generated by the binary spiral axicon for different transverse periods: (a)  $p = 37.00 \mu\text{m}$ , (b)  $p = 89.00 \mu\text{m}$ , (c)  $p = 168.50 \mu\text{m}$ , and (d)  $p = 300.00 \mu\text{m}$ . A decrease of the period enhances the dominance of a single  $\ell$  component, whereas larger periods lead to pronounced mixing of opposite topological charges and the formation of symmetric  $\pm\ell$  superpositions. All other parameters are kept fixed.

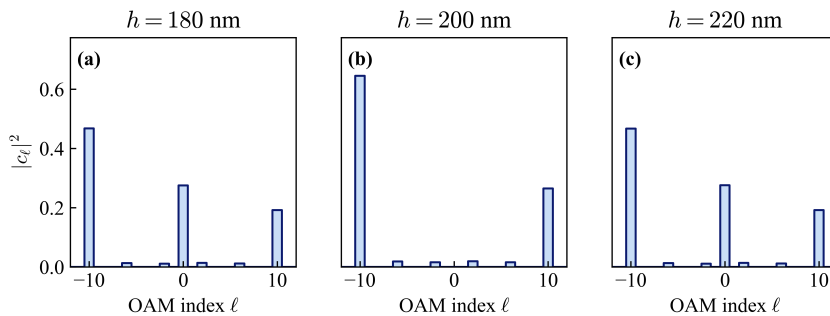


**Figure 11:** Projected OAM spectra  $|c_\ell|^2$  of the field generated by the binary spiral axicon for different SU-8 thicknesses: (a)  $h = 180 \text{ nm}$ , (b)  $h = 200 \text{ nm}$ , and (c)  $h = 220 \text{ nm}$ . Variation of the phase modulation depth leads to the appearance of a non-negligible  $\ell = 0$  component and a redistribution of the relative weights of the  $\pm\ell$  harmonics. All other parameters are kept fixed.

## 4 Experimental results and beam imaging

### 4.1 Experimental setup

Figure 12 shows the optical setup used to characterize the fabricated DOEs. The ultraviolet beam at the wavelength of  $\lambda = 260\text{--}266 \text{ nm}$  was extracted from the photoinjector transport line using a secondary periscope and directed through a spatial filtering stage consisting of a focusing lens and a  $200 \mu\text{m}$  pinhole. For measurements involving the fork grating, an additional focusing lens was introduced to provide tighter illumination of the DOE.

After spatial filtering, the beam illuminated the DOE under test (fork grating, SPP, or axicon). For the OAM diagnostics in the fork-grating and SPP experiments, a cylindrical lens with a focal length of 100 mm was used to perform Laguerre–Gaussian to Hermite–Gaussian (LG-to-HG) mode conversion [44, 45]. The resulting intensity distributions were recorded with a UV-sensitive SDU-285R CCD camera.

This optical layout also enables the formation of a Gaussian beam with a transverse diameter of approximately  $800 \mu\text{m}$  and low angular divergence, suitable for subsequent illumination of photocathodes or additional diagnostics.

### 4.2 Experiments with fork grating

The reflective fork grating was first tested using the UV beam prepared by the spatial-filtering stage. The generated twisted light beams are shown in Figure 13. In these measurements, the central (zeroth-order) beam was blocked to avoid saturation of the CCD sensor. As expected for a grating with  $m = 2$ , the  $\pm 1$  and  $\pm 2$  diffraction orders produced Laguerre–Gaussian modes with orbital angular momenta  $\ell = \pm 2$  and  $\ell = \pm 4$ , respectively. Power measurements using an Ophir 3A-FS detector confirmed that the majority of the transmitted energy was contained in the zeroth and first diffraction orders, while higher

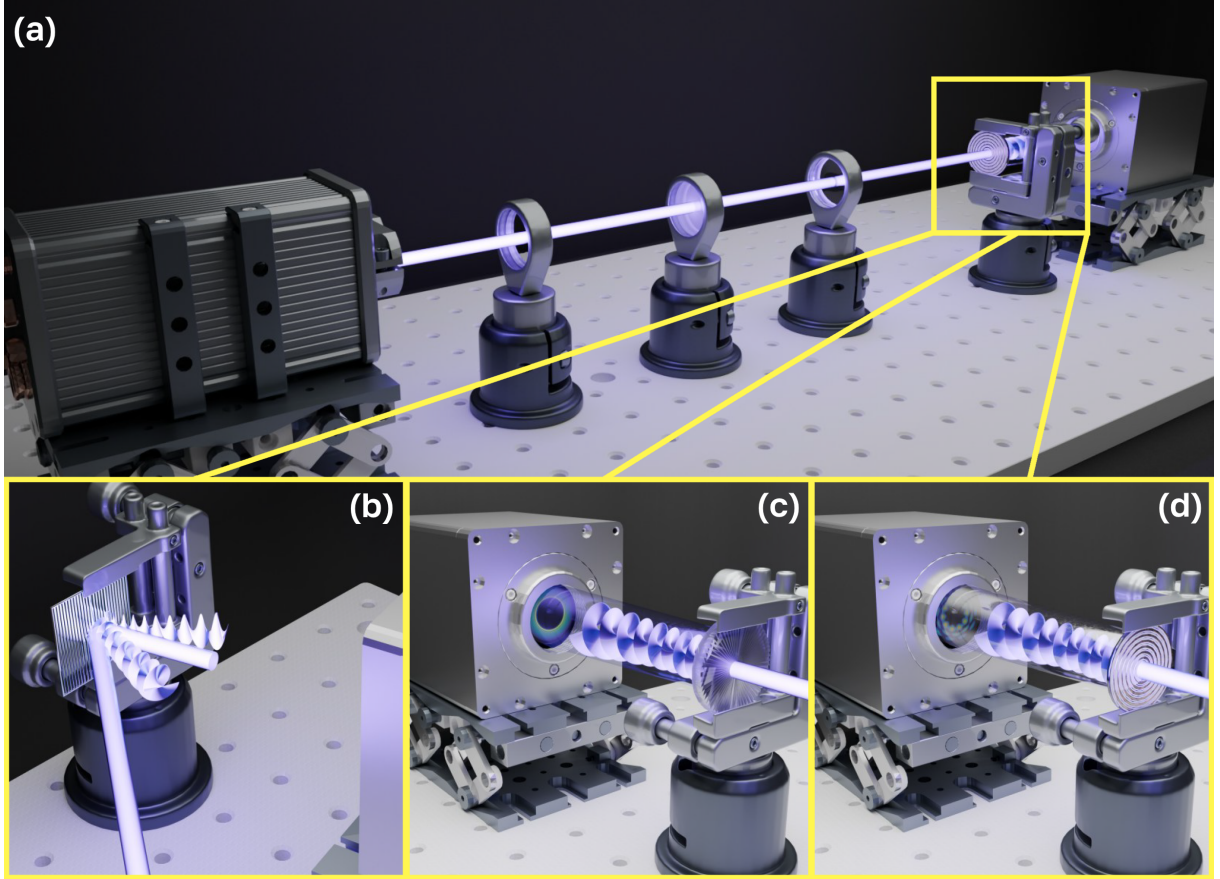


**Figure 12:** Schematic layout of the experimental setup and representative beam-formation configurations. (a) General view of the optical experiment, including the drive laser beamline, beam-conditioning optics, and the detection system. (b) Diffraction of the laser beam by a reflective fork grating, yielding Laguerre–Gaussian modes in several diffraction orders with topological charges proportional to the grating topological charge  $m = 2$ . (c) Generation of twisted light carrying orbital angular momentum  $\ell = 64\hbar$  using a spiral phase plate (SPP). (d) Formation of a coherent superposition of quasi-Bessel twisted light modes produced by a binary axicon.

orders much less visible.

The corresponding Hermite–Gaussian modes obtained after cylindrical-lens conversion are presented in Figure 13(b). The observed modal structures agree with the expected relation [44, 45]

$$N = |\ell| + 1, \quad (13)$$

demonstrating that the grating reliably generates the targeted OAM states. Higher diffraction orders ( $n = -3$  and  $n = -4$ ), shown in Figure 13(c) and (d), also exhibit well-defined modal patterns, confirming correct operation of the fabricated structure across multiple orders.

A potential route for improving the performance of the diffractive element is to increase the spatial resolution of the grating lines. A finer grating would enable the generation of higher-quality vortex modes but would also require tighter focusing of the incident beam onto the grating surface. Overall, the experimentally measured spatial profiles in Figure 13(a) and (b) show good qualitative agreement with the simulations presented in Figure 6, confirming correct operation of the fabricated fork grating.

### 4.3 Experiments with SPP

The next experiment was performed using the fabricated SPP, and the resulting beam profiles are shown in Figure 14(a) and (b). The output twisted light (see Figure 14(a)) exhibits a well-defined annular structure with a pronounced central singularity. A portion of the beam energy is redistributed into several weak concentric rings surrounding the primary vortex mode, consistent with the expected behavior of high-charge SPP-generated beams.

Power measurements performed with the Ophir 3A-FS detector showed an intensity reduction of approximately 20%. Although this differs from the theoretical conversion efficiency of  $\sim 90\%$ , the obtained

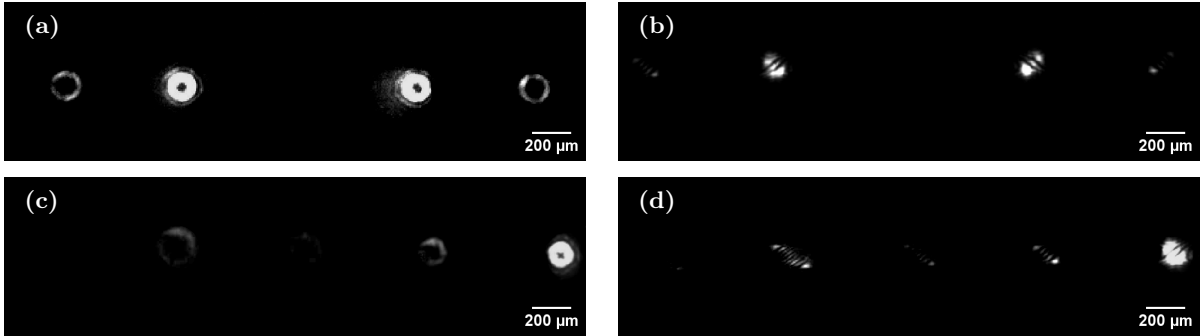


**Figure 13:** Twisted light generated by the reflective fork grating. (a) Laguerre–Gaussian modes with the OAM  $\ell = \pm 2$  and  $\ell = \pm 4$  observed in the  $\pm 1$  and  $\pm 2$  diffraction orders. (b) Corresponding Hermite–Gaussian modes obtained after cylindrical-lens mode conversion. (c) Higher-order Laguerre–Gaussian modes with  $\ell = -2, -4, -6, -8$  observed in the  $n = -1, -2, -3, -4$  diffraction orders. (d) Corresponding Hermite–Gaussian modes obtained after cylindrical-lens mode conversion.

value is still reasonable given the surface-profile discretization, potential scattering losses, and alignment constraints in the UV. The measured twisted light structure and transverse size closely match the simulated pattern shown in Figure 7.

The Hermite–Gaussian mode (see Figure 14(b)) exhibits a slightly larger tilt compared with the simulation. This effect is attributed to a small intentional misalignment of the beam relative to the focal plane of the cylindrical lens, introduced to improve the separation and visibility of the experimentally observed mode stripes.

#### 4.4 Experiments with binary axicons

The final series of experiments was performed using the fabricated binary axicons. The resulting quasi–Bessel beams are shown in Figure 14(c) and (d). For the axicon with the topological charge  $m = 3$  (see Figure 14(c)), three intensity lobes are clearly visible, consistent with the expected topological charge. At short propagation distances, these lobes partially overlap and form a characteristic Y-shaped pattern, which is typical for binary axicons due to the limited spatial separation between the initial diffraction maxima.

In contrast, the axicon with  $m = 10$  produces a well-resolved multi-lobe ring (see Figure 14(d)), in good agreement with the simulated patterns in Figure 8. Both axicons exhibit weak spiral-like background features associated with the binary phase discretization.

Measured power losses did not exceed 30%, indicating high transmission and good mode quality. As the propagation distance increased, the ring radius expanded while the internal lobe structure remained nearly unchanged, consistent with the expected behavior of quasi–Bessel beams with low angular divergence.

Finally, we note that Bessel and quasi–Bessel beams cannot be converted into Hermite–Gaussian modes using a cylindrical-lens scheme, since their propagation-invariant structure does not undergo the conventional LG-to-HG transformation. For such beams, the orbital angular momentum projection simply coincides with the topological charge  $m$ . As shown in Ref. [22],  $m$  can be obtained simply by counting the number of intensity maxima in the ring, providing a straightforward and reliable method for identifying the OAM content of quasi–Bessel beams. In practice, quasi–Bessel beams can exhibit a finite OAM bandwidth due to small contributions the nearby OAM states, but the mean topological charge still equals to  $m$ , as discussed in Section 3.

## 5 Discussion and conclusion

We have demonstrated the generation and numerical propagation of optical beams carrying orbital angular momentum in the deep-ultraviolet range using fabricated diffractive optical elements, including fork gratings, spiral phase plates, and binary axicons. A consistent angular-spectrum–based modeling approach was used to compare the resulting transverse intensity distributions and modal properties.

Fork gratings generate Laguerre–Gaussian modes with systematically increasing ring radii and well-defined annular profiles, in agreement with the experimental radial distributions shown in Figure 15(a)–(c) and the simulations in Figure 6. Spiral phase plates provide the highest modal purity and conversion efficiency, enabling stable generation of high-order OAM states up to  $\ell = 64$ , as illustrated in Figure 15(d)

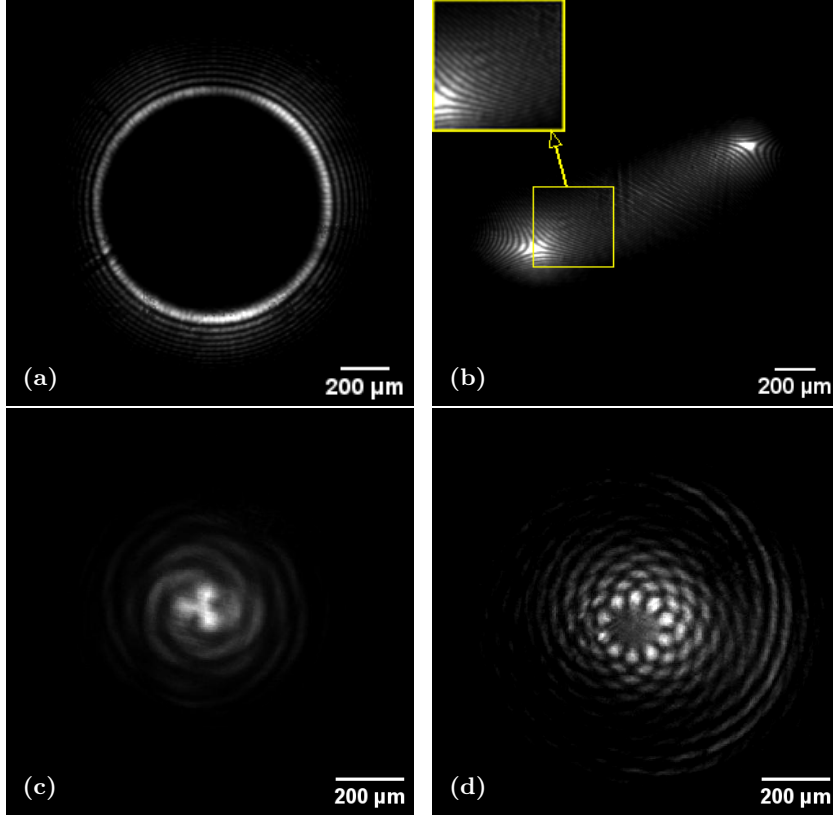


**Figure 14:** Twisted light generated by structured optical elements. (a) Laguerre–Gaussian vortex carrying the OAM  $\ell = 64$  generated by the SPP. (b) Corresponding Hermite–Gaussian mode of the order  $N = 65$  obtained after cylindrical-lens mode conversion. (c) Quasi–Bessel beam produced by the binary axicon with the topological charge  $m = 3$ , exhibiting three intensity lobes. (d) Quasi–Bessel beam produced by the binary axicon with the topological charge  $m = 10$ , exhibiting ten resolved lobes.

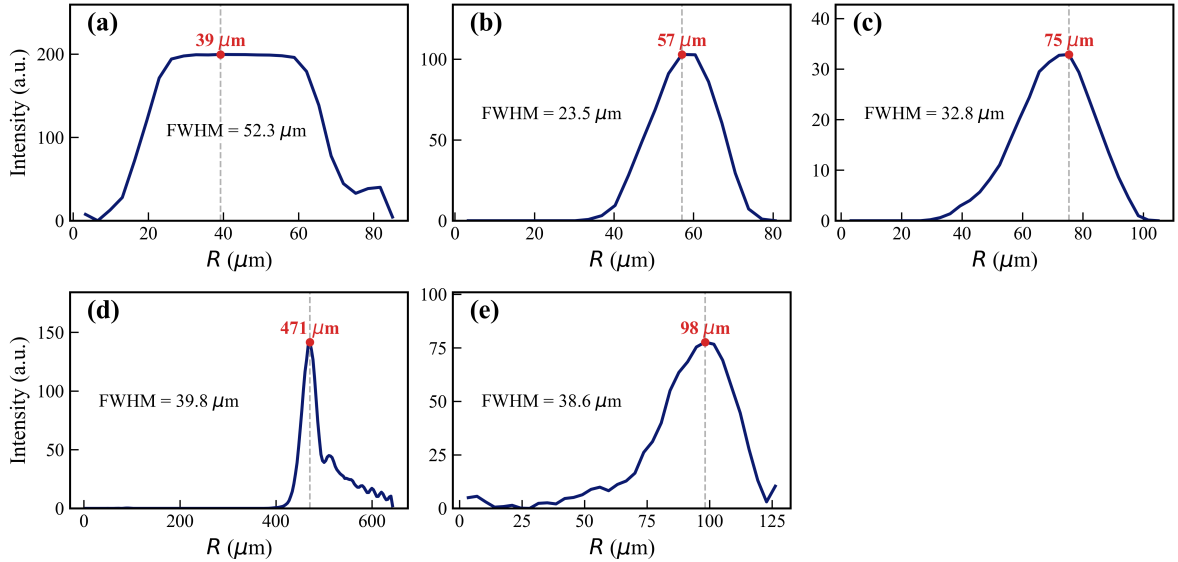


**Figure 15:** Radial profiles of the generated twisted light beams: (a) – (c) – fork grating producing the OAM  $\ell = 2$ ,  $\ell = 4$  and  $\ell = 8$  modes; (d) – SPP generating a high-order LG beam with  $\ell = 64$ ; (e) – binary axicon producing a quasi–Bessel beam with the topological charge  $m = 10$ .

and Figure 7. Binary axicons produce low-divergence quasi–Bessel beams with segmented ring-shaped intensity profiles and a finite OAM bandwidth corresponding to a superposition of multiple OAM states,

consistent with the experimental and numerical results in Figures 15(e) and 8. A comparative overview of the three diffractive elements is summarized in Table 1.

This enables the generation of high-order OAM beams up to  $\ell = 64$  with well-defined transverse structure, suitable for OAM transfer to relativistic electrons [16] and diagnostics in RF photoinjectors. Given that the divergence of Laguerre–Gaussian modes scales as  $\sqrt{\ell}$  [8], beamlines for high-OAM injection must account for the corresponding increase of the Twiss  $\beta$ -function and transverse emittance [46, 47, 48]. For metallic photocathodes, spiral phase plates and axicons are particularly attractive due to their higher efficiency, modal purity, and power handling. The high modal purity of the SPP beam also facilitates OAM diagnostics based on LG–HG conversion using astigmatic optics [49], while diffraction on a triangular aperture provides a viable alternative for quasi–Bessel beams generated by axicons [50]. Overall, the presented results establish a direct connection between diffractive phase design, numerical propagation, and structured light generation in the DUV regime, relevant for photocathode-based RF photoinjectors and accelerator-driven applications.

Parameter	Fork Grating	SPP	Axicon
Fabrication complexity	Low	Very High	High
DUV compatibility	Good	Very High	Very High
Efficiency	60%	80%	70%
Cost	Low	Very High	Mid
Mode Quality	High	Very High	High
Suggested Photocathode Type	Semiconductor	Any Type	Any Type

**Table 1:** Comparison of parameters for the fork grating, the spiral phase plate, and the binary axicon.

### Acknowledgements

We deeply acknowledge A.A. Bogdanov for the help that made the fabrication of the spiral phase plate possible. We sincerely thank K.V. Cherepanov for invaluable assistance and advice. We are also grateful to S.S. Baturin for helpful discussions and constructive feedback. We additionally thank N.E. Sheremet for assistance with developing the numerical code used to generate the fork-grating phase masks. The axicons were simulated and fabricated at the shared research facility of Siberian Center for Synchrotron and Terahertz Radiation at the basis of the Novosibirsk Free Electron Laser, Budker Institute of Nuclear Physics SB RAS. The authors sincerely thank Maria Zhuravleva for her valuable assistance in preparing the graphical materials for this work.

This study was supported by the Russian Science Foundation (Project No. 23-62-10026) [1].

## References

- [1] Russian Science Foundation (Project No. 23-62-10026), <https://rscf.ru/en/project/23-62-10026/>.
- [2] L. Allen, M. W. Beijersbergen, R. J. C. Spreeuw, J. P. Woerdman, Orbital angular momentum of light and the transformation of laguerre-gaussian laser modes, *Phys. Rev. A* 45 (1992) 8185–8189. [doi:10.1103/PhysRevA.45.8185](https://doi.org/10.1103/PhysRevA.45.8185).
- [3] D. L. Andrews, M. Babiker, *The Angular Momentum of Light*, 1st Edition, Cambridge University Press, 2012. [doi:10.1017/CB09780511795213](https://doi.org/10.1017/CB09780511795213).
- [4] S. Franke-Arnold, L. Allen, M. Padgett, Advances in optical angular momentum, *Laser & Photonics Reviews* 2 (4) (2008) 299–313. [doi:https://doi.org/10.1002/lpor.200810007](https://doi.org/10.1002/lpor.200810007).
- [5] K. Bliokh, I. Ivanov, G. Guzzinati, L. Clark, R. Van Boxem, A. B  ch  , R. Juchtmans, M. Alonso, P. Schattschneider, F. Nori, J. Verbeeck, Theory and applications of free-electron vortex states, *Physics Reports* 690 (2017) 1–70, theory and applications of free-electron vortex states. [doi:https://doi.org/10.1016/j.physrep.2017.05.006](https://doi.org/10.1016/j.physrep.2017.05.006).
- [6] M. Babiker, D. L. Andrews, V. E. Lembessis, Atoms in complex twisted light, *Journal of Optics* 21 (1) (2018) 013001. [doi:10.1088/2040-8986/aaed14](https://doi.org/10.1088/2040-8986/aaed14).
- [7] K. Floetmann, D. Karlovets, Quantum mechanical formulation of the busch theorem, *Phys. Rev. A* 102 (2020) 043517. [doi:10.1103/PhysRevA.102.043517](https://doi.org/10.1103/PhysRevA.102.043517).

- [8] D. Karlovets, Vortex particles in axially symmetric fields and applications of the quantum busch theorem, *New Journal of Physics* 23 (3) (2021) 033048. doi:10.1088/1367-2630/abeacc.
- [9] I. P. Ivanov, Promises and challenges of high-energy vortex states collisions, *Progress in Particle and Nuclear Physics* 127 (2022) 103987. doi:https://doi.org/10.1016/j.pnpnp.2022.103987.
- [10] S. Fu, C. Gao, *Optical Vortex Beams: Fundamentals and Techniques*, 1st Edition, Springer Singapore, 2024. doi:10.1007/978-981-99-1810-2.
- [11] A. Schimmoller, S. Walker, A. S. Landsman, Photonic angular momentum in intense light-matter interactions, *Photonics* 11 (9) (2024). doi:10.3390/photonics11090871.
- [12] F. Brandt, M. Hiekkamäki, F. Bouchard, M. Huber, R. Fickler, High-dimensional quantum gates using full-field spatial modes of photons, *Optica* 7 (2) (2020) 98–107. doi:10.1364/OPTICA.375875.
- [13] R. Fickler, F. Bouchard, E. Giese, V. Grillo, G. Leuchs, E. Karimi, Full-field mode sorter using two optimized phase transformations for high-dimensional quantum cryptography, *Journal of Optics* 22 (2) (2020) 024001. doi:10.1088/2040-8986/ab6303.
- [14] H. Cao, S.-C. Gao, C. Zhang, J. Wang, D.-Y. He, B.-H. Liu, Z.-W. Zhou, Y.-J. Chen, Z.-H. Li, S.-Y. Yu, J. Romero, Y.-F. Huang, C.-F. Li, G.-C. Guo, Distribution of high-dimensional orbital angular momentum entanglement over a 1-km few-mode fiber, *Optica* 7 (3) (2020) 232–237. doi:10.1364/OPTICA.381403.
- [15] A. Denoeud, L. Chopineau, A. Leblanc, F. Quéré, Interaction of ultraintense laser vortices with plasma mirrors, *Phys. Rev. Lett.* 118 (2017) 033902. doi:10.1103/PhysRevLett.118.033902.
- [16] I. I. Pavlov, A. D. Chaikovskaia, D. V. Karlovets, Generation of vortex electrons by atomic photoionization, *Phys. Rev. A* 110 (2024) L031101. doi:10.1103/PhysRevA.110.L031101.
- [17] A. S. Dyatlov, M. A. Nozdrin, A. N. Sergeev, N. E. Sheremet, S. S. Stafeev, D. V. Karlovets, Generation of deep ultraviolet vortices via amplitude and phase spiral zone plates, *Appl. Opt.* 64 (36) (2025) 10776–10780. doi:10.1364/AO.578189.
- [18] A. I. Solomonov, O. M. Kushchenko, K. I. Kasyanova, S. B. Isaeva, I. I. Shishkin, D. Y. Terekhov, P. I. Lazarenko, M. V. Rybin, S. S. Baturin, A. D. Sinelnik, Switching topological charge of optical vortex by two-dimensional structures, *Applied Materials Today* 37 (2024) 102135. doi:10.1016/j.apmt.2024.102135.
- [19] S. N. Khonina, V. V. Podlipnov, S. V. Karpeev, A. V. Ustinov, S. G. Volotovskiy, S. V. Ganchevskaya, Spectral control of the orbital angular momentum of a laser beam based on 3d properties of spiral phase plates fabricated for an infrared wavelength, *Opt. Express* 28 (12) (2020) 18407–18417. doi:10.1364/OE.396199.
- [20] S. S. R. Oemrawsingh, J. A. W. van Houwelingen, E. R. Eliel, J. P. Woerdman, E. J. K. Verstegen, J. G. Kloosterboer, G. W. 't Hooft, Production and characterization of spiral phase plates for optical wavelengths, *Appl. Opt.* 43 (3) (2004) 688–694. doi:10.1364/AO.43.000688.
- [21] N. Osintseva, V. Gerasimov, B. Knyazev, M. Komlenok, V. Pavelyev, D. Yablokov, Terahertz besel and "perfect" vortex beams generated with a binary axicon and axicon with continuous relief, *Computer Optics* 3 (46) (2022) 375–380. doi:10.18287/2412-6179-CO-1066.
- [22] B. Knyazev, N. Osintseva, M. Komlenok, V. Pavelyev, V. Gerasimov, O. Kameshkov, Y. Choporova, K. Tukmakov, Terahertz besel beams formed by binary and holographic axicons, *Photonics* 10 (6) (2023). doi:10.3390/photonics10060700.
- [23] N. Bazdyrev, V. Gerasimov, V. Pavelyev, A. Agafonov, K. Tukmakov, Techniques to estimate zone of formation of terahertz besel vortex beams, *Journal of Infrared, Millimeter, and Terahertz Waves* 47 (46) (2025). doi:10.1007/s10762-025-01066-4.
- [24] E. I. Gacheva, A. K. Poteomkin, E. A. Khazanov, V. V. Zelenogorskii, E. V. Katin, G. A. Luchinin, N. I. Balalykin, V. F. Minashkin, M. A. Nozdrin, G. V. Trubnikov, G. D. Shirkov, Laser driver for a photoinjector of an electron linear accelerator, *IEEE Journal of Quantum Electronics* 50 (7) (2014) 522–529. doi:10.1109/JQE.2014.2323472.

- [25] P. Schattschneider, B. Schaffer, I. Ennen, J. Verbeeck, Mapping spin-polarized transitions with atomic resolution, *Phys. Rev. B* 85 (2012) 134422. doi:10.1103/PhysRevB.85.134422.
- [26] Y. Wu, L. Ji, X. Geng, Q. Yu, N. Wang, B. Feng, Z. Guo, W. Wang, C. Qin, X. Yan, L. Zhang, J. Thomas, A. Hützen, M. Büscher, T. P. Rakitzis, A. Pukhov, B. Shen, R. Li, Polarized electron-beam acceleration driven by vortex laser pulses, *New Journal of Physics* 21 (7) (2019) 073052. doi:10.1088/1367-2630/ab2fd7.
- [27] F. An, D. Bai, H. Cai, S. Chen, X. Chen, H. Duyang, L. Gao, S. Ge, J. He, J. Huang, Z. Huang, I. Ivanov, C. Ji, H. Jia, J. Jiang, X. Kang, S.-B. Kim, C. Kong, W. Kou, Q. Li, Q. Li, J. Liao, J. Ling, C.-E. Liu, X. Ma, H. Qiu, J. Tang, R. Wang, W. Wen, J. Wu, J. Xiao, X. Xiao, Y. Xu, W. Yang, X. Yang, J. Yao, Y. Yuan, M. Zaiba, P. Zhang, S. Zhang, S. Zhang, S. Zhao, L. Zou, High-precision physics experiments at huizhou large-scale scientific facilities, *Chinese Physics Letters* 42 (11) (2025) 110102. doi:10.1088/0256-307X/42/11/110102.
- [28] V. V. Kotlyar, A. A. Kovalev, A. G. Nalimov, *Topological Charge of Optical Vortices*, 1st Edition, Taylor & Francis Group, 2022. doi:10.1201/9781003326304.
- [29] B. Goebel, L. L. Wang, T. Tschudi, Multilayer technology for diffractive optical elements, *Appl. Opt.* 35 (22) (1996) 4490–4493. doi:10.1364/AO.35.004490.
- [30] X. Wang, J. R. Leger, R. H. Rediker, Rapid fabrication of diffractive optical elements by use of image-based excimer laser ablation, *Appl. Opt.* 36 (20) (1997) 4660–4665. doi:10.1364/AO.36.004660.
- [31] G. Kostyuk, V. Shkuratova, A. Petrov, D. Mesheryakov, K. Eliseev, D. Stepanyuk, Multisector binary phase plates on fused silica for generation of optical vortex beams superposition: Fabrication, characterization, and applications, *Optics & Laser Technology* 152 (2022) 108161. doi:https://doi.org/10.1016/j.optlastec.2022.108161.
- [32] C. Shi, W. Zhao, S. Chen, W. Li, Multilevel diffractive lenses: Recent advances and applications, *Symmetry* 16 (10) (2024). doi:10.3390/sym16101377.
- [33] O. E. Kameshkov, B. A. Knyazev, Simulating diffraction on a series of amplitude-phase masks for experiments at the novosibirsk free electron laser, *Bulletin of the Russian Academy of Sciences: Physics* 83 (2) (2019) 184–189. doi:10.3103/S1062873819020175.
- [34] J. Goodman, *Introduction to Fourier optics*, 3rd Edition, Roberts & Co. Publishers, 2005.
- [35] V. Nazmov, E. Reznikova, J. Mohr, A. Snigirev, I. Snigireva, S. Achenbach, V. Saile, Fabrication and preliminary testing of x-ray lenses in thick su-8 resist layers, *Microsystem Technologies* 10 (10) (2004) 716–721. doi:10.1007/s00542-004-0433-0.
- [36] R. Vasilyeu, A. Dudley, N. Khilo, A. Forbes, Generating superpositions of higher-order bessel beams, *Opt. Express* 17 (26) (2009) 23389–23395. doi:10.1364/OE.17.023389.
- [37] A. A. Kovalev, V. V. Kotlyar, A. P. Porfirev, Shifted nondiffractive bessel beams, *Phys. Rev. A* 91 (2015) 053840. doi:10.1103/PhysRevA.91.053840.
- [38] F. Saadati-Sharafteh, A. Borhanifar, A. P. Porfirev, P. Amiri, E. A. Akhlaghi, S. N. Khonina, Y. Azizian-Kalandaragh, The superposition of the bessel and mirrored bessel beams and investigation of their self-healing characteristic, *Optik* 208 (2020) 164057. doi:https://doi.org/10.1016/j.ijleo.2019.164057.
- [39] P. Carruthers, M. M. Nieto, Phase and angle variables in quantum mechanics, *Rev. Mod. Phys.* 40 (1968) 411–440. doi:10.1103/RevModPhys.40.411.
- [40] L. Torner, J. P. Torres, S. Carrasco, Digital spiral imaging, *Opt. Express* 13 (3) (2005) 873–881. doi:10.1364/OPEX.13.000873.
- [41] M. V. Vasnetsov, V. A. Pas'ko, M. S. Soskin, Analysis of orbital angular momentum of a misaligned optical beam, *New Journal of Physics* 7 (1) (2005) 46. doi:10.1088/1367-2630/7/1/046.
- [42] M. M. Sánchez-López, I. Moreno, J. A. Davis, B. K. Gutierrez, D. M. Cottrell, Double-ring interference of binary diffractive axicons, *OSA Continuum* 3 (6) (2020) 1679–1690. doi:10.1364/OSAC.393734.

- [43] S. Fu, Z. Shang, L. Hai, L. Huang, Y. Lv, C. Gao, Orbital angular momentum comb generation from azimuthal binary phases, *Advanced Photonics Nexus* 1 (1) (2022) 016003. doi:[10.1117/1.APN.1.1.016003](https://doi.org/10.1117/1.APN.1.1.016003).
- [44] M. Beijersbergen, L. Allen, H. van der Veen, J. Woerdman, Astigmatic laser mode converters and transfer of orbital angular momentum, *Optics Communications* 96 (1) (1993) 123–132. doi:[10.1016/0030-4018\(93\)90535-D](https://doi.org/10.1016/0030-4018(93)90535-D).
- [45] V. V. Kotlyar, A. A. Kovalev, A. P. Porfirev, Astigmatic transforms of an optical vortex for measurement of its topological charge, *Appl. Opt.* 56 (14) (2017) 4095–4104. doi:[10.1364/AO.56.004095](https://doi.org/10.1364/AO.56.004095).
- [46] H. Wiedemann, *Particle Accelerator Physics*, 4th Edition, Springer Cham, 2015. doi:[10.1007/978-3-319-18317-6](https://doi.org/10.1007/978-3-319-18317-6).
- [47] A. W. Chao, *Lectures on Accelerator Physics*, 1st Edition, World Scientific, 2020. doi:[10.1142/12004](https://doi.org/10.1142/12004).
- [48] S. Y. Lee, *Accelerator Physics*, 4th Edition, World Scientific Publishing Company, 2021. doi:[10.1142/11111](https://doi.org/10.1142/11111).
- [49] P. Schattschneider, M. Stöger-Pollach, J. Verbeeck, Novel vortex generator and mode converter for electron beams, *Phys. Rev. Lett.* 109 (2012) 084801. doi:[10.1103/PhysRevLett.109.084801](https://doi.org/10.1103/PhysRevLett.109.084801).
- [50] M. Maksimov, N. Borodin, D. Kargina, D. Naumov, D. Karlovets, Diffraction by circular and triangular apertures as a diagnostic tool of twisted matter waves, *Phys. Rev. A* 112 (2025) 062823. doi:[10.1103/z2rs-2ryl](https://doi.org/10.1103/z2rs-2ryl).